Computers and Mathematics with Applications 73 (2017) 2388–2403

Contents lists available at ScienceDirect

Computers and Mathematics with Applications

journal homepage: www.elsevier.com/locate/camwa

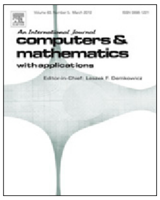

Convex Splitting Runge–Kutta methods for phase-field models

Jaemin Shin [a], Hyun Geun Lee [b], June-Yub Lee [c,*]

[a] *Institute of Mathematical Sciences, Ewha Womans University, Seoul 03760, Republic of Korea*
[b] *Department of Mathematics, Kwangwoon University, Seoul 01897, Republic of Korea*
[c] *Department of Mathematics, Ewha Womans University, Seoul 03760, Republic of Korea*

ARTICLE INFO

Article history:
Received 1 February 2016
Received in revised form 31 March 2017
Accepted 3 April 2017
Available online 20 April 2017

Keywords:
Convex splitting
Implicit–explicit Runge–Kutta
Allen–Cahn equation
Cahn–Hilliard equation
Phase-field crystal equation

ABSTRACT

In this paper, we present the Convex Splitting Runge–Kutta (CSRK) methods which provide a simple unified framework to solve phase-field models such as the Allen–Cahn, Cahn–Hilliard, and phase-field crystal equations. The core idea of the CSRK methods is the combination of convex splitting methods and multi-stage implicit–explicit Runge–Kutta methods. Our CSRK methods are high-order accurate in time and we investigate the energy stability numerically. We present numerical experiments to show the accuracy and efficiency of the proposed methods up to the third-order accuracy.

1. Introduction

Phase-field models have emerged as a powerful computational approach for modeling and predicting mesoscale morphological and microstructure evolution in materials. The most popular models are the Allen–Cahn (AC) [1] and Cahn–Hilliard (CH) [2] equations with non-conserved or conserved order parameters ϕ that vary continuously over thin interfacial layers and are mostly uniform in the bulk phases [3]. The equations are derived from the Ginzburg–Landau free energy:

$$\mathcal{E}(\phi) = \int_{\Omega} \left(\Psi(\phi) + \frac{\epsilon^2}{2}|\nabla\phi|^2 \right) d\mathbf{x}, \tag{1}$$

where Ω is a domain in $\mathbb{R}^d$ $(d = 1, 2, 3)$, $\Psi(\phi)$ is the bulk free energy with two minima corresponding to the two phases, and $\epsilon > 0$ is a parameter related to the interfacial thickness. The AC and CH equations are the gradient flow for (1) under the L^2 and H^{-1} inner product, respectively. The equations have previously been applied to a wide range of physical problems [4].

The most significant difficulties in solving phase-field models are their nonlinear and high-order derivative terms, since they cause a severe restriction on the time step size for stability. In order to overcome this problem, the authors in [5,6] proposed the first-order convex splitting method. In the method, $\mathcal{E}(\phi)$ is split appropriately into a contractive part and an expansive part:

$$\mathcal{E}(\phi) = \int_{\Omega} \left(\Psi_c(\phi) + \frac{\epsilon^2}{2}|\nabla\phi|^2 \right) d\mathbf{x} - \int_{\Omega} \Psi_e(\phi)\, d\mathbf{x} = \mathcal{E}_c(\phi) - \mathcal{E}_e(\phi), \tag{2}$$

---

[*] Corresponding author.
E-mail address: jyllee@ewha.ac.kr (J.-Y. Lee).

http://dx.doi.org/10.1016/j.camwa.2017.04.004
0898-1221/

where both $\mathcal{E}_c(\phi)$ and $\mathcal{E}_e(\phi)$ are convex. Also, $\mathcal{E}_c(\phi)$ is treated implicitly, whereas $\mathcal{E}_e(\phi)$ is treated explicitly. The first-order method has been proven to be unconditionally energy stable, which means that $\mathcal{E}(\phi)$ is non-increasing in time for any time step. Since the method is only first-order accurate in time, a number of second-order methods have been proposed considering the energy stability. For example, the schemes in [7–9] are based on the convex splitting and multi-step discretization and the schemes in [10,11] are based on the Crank–Nicolson type scheme with convex splitting and stabilization. Many other attempts have also been made to achieve high-order accuracy without using a convex splitting scheme [12–19]. However, only a limited number of high-order methods guarantee energy stability [18].

In this paper, we present the Convex Splitting Runge–Kutta (CSRK) methods in order to provide a simple unified framework to solve phase-field models with high-order time accuracy. The core idea of the methods is to couple convex splitting methods described in Section 2 with the multi-stage implicit–explicit Runge–Kutta (IMEX-RK) methods described in Section 3. In Section 4.1, it is numerically shown that the convexity of splitting is crucial to ensure the energy stability of the CSRK methods. We investigate the order of accuracy and stability of the CSRK methods depending on the IMEX-RK tables described in Sections 4.2 and 4.3. In Section 5, we numerically demonstrate the order of accuracy with typical spinodal decomposition examples. We also simulate further complex examples to show the applicability and feasibility of the proposed method. Finally, conclusions are drawn in Section 6. We briefly introduce the derivation of order conditions in Appendix A and provide some specific examples in Appendix B. It is worth to note that spectral methods similar to those in [16,9] are used for spatial discretization in our numerical computations.

2. First-order convex splitting method

Phase-field models such as the AC and CH equations are characterized by a bulk free energy $\Psi(\phi)$ and an interfacial energy $\frac{\epsilon^2}{2}|\nabla\phi|^2$. Time discretization methods have to deal with the nonlinear term $\Psi'(\phi)$ which yields a severe stability restriction on the time step. This stability issue has motivated a large number of studies in which schemes are developed that are provably energy stable.

In this section, we briefly review the convex splitting method, which is a successful attempt to overcome the stability restriction. For simplicity, we consider the AC or CH equation as follows:

$$\frac{\partial\phi}{\partial t} = \mathcal{L}\left(\Psi'(\phi) - \epsilon^2\Delta\phi\right), \tag{3}$$

where $\mathcal{L} = -1$ for AC or $\mathcal{L} = \Delta$ for CH. With the energy splitting (2), the first-order convex splitting method is

$$\frac{\phi^{n+1} - \phi^n}{\Delta t} = \mathcal{L}\left(\Psi_c'(\phi^{n+1}) - \epsilon^2\Delta\phi^{n+1} - \Psi_e'(\phi^n)\right). \tag{4}$$

Considering a typical polynomial energy $\Psi(\phi) = \frac{1}{4}(\phi^2 - 1)^2$, nonlinear convex splitting can be given as follows:

$$\Psi_c(\phi) = \frac{1}{4}\phi^4 + \frac{1}{4}, \qquad \Psi_e(\phi) = \frac{1}{2}\phi^2. \tag{5}$$

Applying the nonlinear convex splitting (5), we have

$$\frac{\phi^{n+1} - \phi^n}{\Delta t} = \mathcal{L}\left(\left(\phi^{n+1}\right)^3 - \epsilon^2\Delta\phi^{n+1} - \phi^n\right). \tag{6}$$

In order to treat the nonlinearity of ϕ^3, we consider a Newton-type iterative method. Using the mth Newton's iteration $\phi^{n,m}$ of ϕ^{n+1}, we linearize the nonlinear term $\left(\phi^{n+1}\right)^3$ as follows,

$$\left(\phi^{n+1}\right)^3 \approx \left(\phi^{n,m}\right)^3 + 3\left(\phi^{n,m}\right)^2\left(\phi^{n+1} - \phi^{n,m}\right) \tag{7}$$

for $m = 0, 1, \ldots$. We then get

$$\frac{\phi^{n,m+1} - \phi^n}{\Delta t} = \mathcal{L}\left(3\left(\phi^{n,m}\right)^2\phi^{n,m+1} - 2\left(\phi^{n,m}\right)^3 - \epsilon^2\Delta\phi^{n,m+1} - \phi^n\right) \tag{8}$$

with an initial estimate $\phi^{n,0} = \phi^n$. We then set $\phi^{n+1} = \phi^{n,m+1}$ if a relative l_2-norm of the consecutive error $\frac{\left\|\phi^{n,m+1} - \phi^{n,m}\right\|}{\|\phi^{n,m}\|}$ is less than a given tolerance *tol*.

The nonlinear convex splitting (5) preserves the convexity of $\Psi_c(\phi)$ and $\Psi_e(\phi)$, regardless of the value of ϕ, whereas the splitting is computationally expensive due to the nonlinear iterative steps. Fig. 1 shows the number of m-iterations averaged over the simulation times $T_f = 156.25$ and $T_f = 156.25 \cdot \epsilon^2$ as a function of Δt and $\Delta\tau = \Delta t/\epsilon^2$ for the AC and CH equations with zero Neumann boundary condition, respectively. Here, an initial condition on a domain $\Omega = [0, 1]$ is $\phi(x, 0) = 0.001 \cdot \mathrm{rand}(x)$, where $\mathrm{rand}(x)$ is a random number between -1 and 1, and $\epsilon = 0.01$, $\Delta x = 1/128$, $\Delta t = T_f/2^{12}, T_f/2^{11}, \ldots, T_f/2^3$, and $tol = 10^{-10}$.

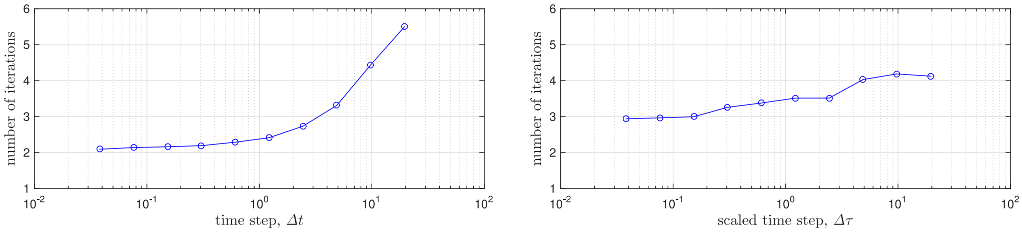

(a) AC equation.

(b) CH equation.

Fig. 1. Number of m-iterations averaged over the simulation time up to T_f. The scaled time step $\Delta\tau$ is defined as $\Delta\tau = \Delta t/\epsilon^2$.

An alternative splitting of $\Psi(\phi)$ is the linear convex splitting as follows

$$\Psi_c(\phi) = \phi^2 + \frac{1}{4}, \qquad \Psi_e(\phi) = \frac{3}{2}\phi^2 - \frac{1}{4}\phi^4. \tag{9}$$

Applying the linear convex splitting, (4) becomes

$$\frac{\phi^{n+1} - \phi^n}{\Delta t} = \mathcal{L}\left(2\phi^{n+1} - \epsilon^2\Delta\phi^{n+1} - 3\phi^n + (\phi^n)^3\right). \tag{10}$$

This is linear for ϕ^{n+1} and we expect to reduce the computational cost compared to the nonlinear convex splitting. Note that, because both $\Psi_c(\phi)$ and $\Psi_e(\phi)$ are convex for $\phi \in [-1, 1]$, we will further investigate the stability of this linear splitting scheme in Section 4.

3. Implicit–explicit Runge–Kutta methods

Here, we review the implicit–explicit Runge–Kutta (IMEX-RK) methods, proposed in [20]. Discretization of the spatial derivatives such as (6) and (10) yields a large system of ordinary differential equations. We simply consider the following system:

$$y_t = f(y) + g(y) \quad \text{and} \quad y(0) = y^0. \tag{11}$$

An IMEX-RK scheme for (11) applies an implicit discretization to the term $f(y)$ and an explicit discretization to the term $g(y)$. For $f(y)$, we consider an s-stage implicit scheme with coefficients $\mathbf{A} \in \mathbb{R}^{(s+1)\times(s+1)}$ and $\mathbf{b}, \mathbf{c} \in \mathbb{R}^{s+1}$. In this work, we consider the diagonally implicit Runge–Kutta (DIRK) method for implementation convenience, which means that $a_{ij} = 0$ if $i < j$ and $a_{ii} \neq 0$ for some $i = 1, 2, \ldots, s$. Also, for $g(y)$, we consider an s-stage explicit scheme with coefficients $\hat{\mathbf{A}} \in \mathbb{R}^{(s+1)\times(s+1)}$ and $\hat{\mathbf{b}}, \hat{\mathbf{c}} \in \mathbb{R}^{s+1}$. We denote the s-stage IMEX-RK Butcher tables as

$$\begin{array}{c} \text{IM: } f(y) \\ \begin{array}{c|c} \mathbf{c} & \mathbf{A} \\ \hline & \mathbf{b}^T \end{array} = \begin{array}{c|ccccc} 0 & 0 & 0 & 0 & \cdots & 0 \\ c_1 & 0 & a_{11} & 0 & \cdots & 0 \\ c_2 & 0 & a_{21} & a_{22} & \cdots & 0 \\ \vdots & \vdots & \vdots & \vdots & \ddots & \vdots \\ c_s & 0 & a_{s1} & a_{s2} & \cdots & a_{ss} \\ \hline & 0 & b_1 & b_2 & \cdots & b_s \end{array} \end{array}, \qquad \begin{array}{c} \text{EX: } g(y) \\ \begin{array}{c|c} \hat{\mathbf{c}} & \hat{\mathbf{A}} \\ \hline & \hat{\mathbf{b}}^T \end{array} = \begin{array}{c|ccccc} 0 & 0 & 0 & 0 & \cdots & 0 \\ \hat{c}_1 & \hat{a}_{10} & 0 & 0 & \cdots & 0 \\ \hat{c}_2 & \hat{a}_{20} & \hat{a}_{21} & 0 & \cdots & 0 \\ \vdots & \vdots & \vdots & \vdots & \ddots & \vdots \\ \hat{c}_s & \hat{a}_{s0} & \hat{a}_{s1} & \hat{a}_{s2} & \cdots & 0 \\ \hline & \hat{b}_0 & \hat{b}_1 & \hat{b}_2 & \cdots & \hat{b}_s \end{array} \end{array}. \tag{12}$$

Note that the coefficients $(\hat{\mathbf{c}}, \hat{\mathbf{A}}, \hat{\mathbf{b}})$ are a general Butcher table for the explicit Runge–Kutta (ERK) method historically called an $(s+1)$-stage ERK method. However, we define the initial state as a zero-stage, and will refer to the ERK as s-stage in this paper for consistency with the implicit method.

We denote y^n as the approximation of $y(t^n)$. With a time step size h, one step evolution from t^n to $t^{n+1} = t^n + h$ of the IMEX-RK method is given as follows: we set a zero-stage as $k_0 = f(y_0)$ and $\hat{k}_0 = g(y_0)$, where $y_0 = y^n$. For each stage $i = 1, 2, \ldots, s$, we calculate

$$k_i = f(y_i),\ \hat{k}_i = g(y_i), \quad \text{where } y_i = y_0 + h\sum_{j=1}^{i} a_{ij}k_j + h\sum_{j=0}^{i-1} \hat{a}_{ij}\hat{k}_j. \tag{13}$$

Table 1
Order conditions for IMEX-RK methods up to the third-order accuracy. Here, we define the component-wise product as $\mathbf{x} \odot \mathbf{y} = (x_0 y_0, x_1 y_1, \ldots, x_s y_s)^T$ for $\mathbf{x} = (x_0, x_1, \ldots, x_s)^T$ and $\mathbf{y} = (y_0, y_1, \ldots, y_s)^T$, and $\mathbf{x}^m = \mathbf{x} \odot \mathbf{x}^{m-1}$ for $m > 1$.

Order	Stand-alone conditions		Coupling conditions
	IM	EX	
1	$\mathbf{b} \cdot \mathbf{1} = 1$	$\hat{\mathbf{b}} \cdot \mathbf{1} = 1$	–
2	$\mathbf{b} \cdot \mathbf{c} = 1/2$	$\hat{\mathbf{b}} \cdot \hat{\mathbf{c}} = 1/2$	$\mathbf{b} \cdot \hat{\mathbf{c}} = \hat{\mathbf{b}} \cdot \mathbf{c} = 1/2$
3	$\mathbf{b} \cdot \mathbf{c}^2 = 1/3$	$\hat{\mathbf{b}} \cdot \hat{\mathbf{c}}^2 = 1/3$	$\hat{\mathbf{b}} \cdot \mathbf{c}^2 = \mathbf{b} \cdot \hat{\mathbf{c}}^2 = 1/3$
	$\mathbf{b} \cdot \mathbf{A}\mathbf{c} = 1/6$	$\hat{\mathbf{b}} \cdot \hat{\mathbf{A}}\hat{\mathbf{c}} = 1/6$	$\hat{\mathbf{b}} \cdot (\mathbf{c} \odot \hat{\mathbf{c}}) = \mathbf{b} \cdot (\mathbf{c} \odot \hat{\mathbf{c}}) = 1/3$
			$\mathbf{b} \cdot \mathbf{A}\hat{\mathbf{c}} = \hat{\mathbf{b}} \cdot \hat{\mathbf{A}}\mathbf{c} = 1/6$
			$\mathbf{b} \cdot \hat{\mathbf{A}}\mathbf{c} + \hat{\mathbf{b}} \cdot \mathbf{A}\mathbf{c} = 1/3$
			$\mathbf{b} \cdot \hat{\mathbf{A}}\hat{\mathbf{c}} + \hat{\mathbf{b}} \cdot \mathbf{A}\hat{\mathbf{c}} = 1/3$

For the column vector $\mathbf{y} = (y_0, y_1, \ldots, y_s)^T$, we define the function evaluation as $f(\mathbf{y}) = (f(y_0), f(y_1), \ldots, f(y_s))^T$. Now, we can rewrite $k_0, k_1, \ldots, k_s$ and $\hat{k}_0, \hat{k}_1, \ldots, \hat{k}_s$ as column vectors

$$\mathbf{k} = f(y_0 \mathbf{1} + h(\mathbf{A}\mathbf{k} + \hat{\mathbf{A}}\hat{\mathbf{k}})), \tag{14}$$

$$\hat{\mathbf{k}} = g(y_0 \mathbf{1} + h(\mathbf{A}\mathbf{k} + \hat{\mathbf{A}}\hat{\mathbf{k}})), \tag{15}$$

where we denote by $\mathbf{1} = (1, 1, \ldots, 1)^T \in \mathbb{R}^{s+1}$. We then evaluate the next time approximation y^{n+1} as

$$y^{n+1} = y_0 + h \sum_{j=0}^{s} (b_j k_j + \hat{b}_j \hat{k}_j), \tag{16}$$

which can be written as $y^{n+1} = y_0 + h(\mathbf{b} \cdot \mathbf{k} + \hat{\mathbf{b}} \cdot \hat{\mathbf{k}})$.

Table 1 lists the order conditions for (12) to make (16) first-, second-, and third-order accurate in time. A detailed description of the order conditions for the IMEX-RK methods is presented in Appendix A.

For the IMEX-RK methods, a wide choice of coefficients that satisfy the order conditions is available in Table 1. To simplify the process of selection, we consider

$$\mathbf{c} = \hat{\mathbf{c}}, \tag{17}$$

$$a_{ii} = \gamma, \quad \text{for } i = 1, 2, \ldots, s, \tag{18}$$

where (17) is a canopy node condition [21] and (18) refers to the singly diagonally implicit Runge–Kutta (SDIRK) table [22]. In addition, we focus on the condition of

$$b_i = a_{si} \quad \text{and} \quad \hat{b}_i = \hat{a}_{si}, \quad \text{for } i = 0, 1, \ldots, s, \tag{19}$$

because it is known that (19) renders the A-stable RK method as L-stable [22]. In particular, the solution y^{n+1} is identical to the last internal stage ($y^{n+1} = y_s$) with (19).

We now introduce some families of our IMEX-RK tables up to the third-order which are used in the numerical tests to demonstrate the accuracy and stability of the proposed methods. For more detailed understanding of the construction of the tables, we refer to Appendix B.

First-order table for IMEX-RK(1)

$$\begin{array}{c|cc} 0 & 0 & 0 \\ 1 & 0 & 1 \\ \hline & 0 & 1 \end{array} \qquad \begin{array}{c|cc} 0 & 0 & 0 \\ 1 & 1 & 0 \\ \hline & 1 & 0 \end{array} \tag{20}$$

Second-order table for IMEX-RK(2, $\boldsymbol{\gamma}$)

$$\begin{array}{c|ccc} 0 & 0 & 0 & 0 \\ \gamma & 0 & \gamma & 0 \\ 1 & 0 & 1-\gamma & \gamma \\ \hline & 0 & 1-\gamma & \gamma \end{array} \qquad \begin{array}{c|ccc} 0 & 0 & 0 & 0 \\ \gamma & \gamma & 0 & 0 \\ 1 & 1-\frac{1}{2\gamma} & \frac{1}{2\gamma} & 0 \\ \hline & 1-\frac{1}{2\gamma} & \frac{1}{2\gamma} & 0 \end{array} \tag{21}$$

where $\gamma = \gamma_{\pm} = (2 \pm \sqrt{2})/2$.

Special case of the third-order table for IMEX-RK(3, $\boldsymbol{\gamma}$)

$$\begin{array}{c|ccccc}
0 & 0 & 0 & 0 & 0 & 0\\
\gamma & 0 & \gamma & 0 & 0 & 0\\
c_2 & 0 & a_{21} & \gamma & 0 & 0\\
c_3 & 0 & a_{31} & a_{32} & \gamma & 0\\
1 & 0 & b_1 & b_2 & b_3 & \gamma\\ \hline
 & 0 & b_1 & b_2 & b_3 & \gamma
\end{array}
\qquad
\begin{array}{c|ccccc}
0 & 0 & 0 & 0 & 0 & 0\\
\gamma & \gamma & 0 & 0 & 0 & 0\\
c_2 & \hat{a}_{20} & \hat{a}_{21} & 0 & 0 & 0\\
c_3 & \hat{a}_{30} & \hat{a}_{31} & \hat{a}_{32} & 0 & 0\\
1 & \hat{b}_0 & \hat{b}_1 & \hat{b}_2 & \hat{b}_3 & 0\\ \hline
 & \hat{b}_0 & \hat{b}_1 & \hat{b}_2 & \hat{b}_3 & 0
\end{array} \tag{22}$$

We consider a special case of the third-order methods with one parameter family for γ. Using the algorithms in Appendix B, we can construct SDIRK and then find ERK from SDIRK. Note that, in the case of $\gamma = 1/2$, the IMEX-RK$(3, \gamma)$ is the same as the four-stage, third-order combination (4, 4, 3) table in [23,24].

4. Convex splitting Runge–Kutta methods

In order to develop high-order methods for phase-field models, we propose the Convex Splitting Runge–Kutta (CSRK) scheme which couples a convex splitting with the IMEX-RK methods. In other words, f and g of the IMEX-RK methods (11) correspond to $\mathcal{E}_c$ and $\mathcal{E}_e$ of convex splitting (2), respectively. A similar attempt was made in [23]; however, we extend it to the general framework for the phase-field models. Expecting that the convex splitting positively affects the stability, we numerically investigate the stability region of CSRK up to the third-order accuracy. Note that the CSRK only considers the multi-stage evaluation without the additional stabilization and multi-step discretization [7,10].

We can define a CSRK method by choosing a convex splitting and an IMEX-RK table. We refer to CSRK(n) for an nth order CSRK method. Note that the convex splitting method [5,6] can be considered as CSRK(1). We describe here CSRK$(2, \gamma_\pm)$ using table (21) for the CH equation (3) with $f(\phi) = \Delta\left(\Psi_c'(\phi) - \epsilon^2\Delta\phi\right)$ and $g(\phi) = -\Delta\Psi_e'(\phi)$:

$$\phi_1 = \phi^n + \Delta t a_{11} f(\phi_1) + \Delta t \hat{a}_{10} g(\phi^n), \tag{23}$$

$$\phi_2 = \phi^n + \Delta t\left[a_{21} f(\phi_1) + a_{22} f(\phi_2)\right] + \Delta t\left[\hat{a}_{20} g(\phi^n) + \hat{a}_{21} g(\phi_1)\right], \tag{24}$$

where $a_{11} = \hat{a}_{10} = a_{22} = \gamma_\pm, a_{21} = 1 - a_{22}, \hat{a}_{21} = 1/(2\gamma_\pm), \hat{a}_{20} = 1 - \hat{a}_{21}$, and $\gamma_\pm = (2 \pm \sqrt{2})/2$. Because $b_1 = a_{21}, b_2 = a_{22}, \hat{b}_0 = \hat{a}_{20}$, and $\hat{b}_1 = \hat{a}_{21}$, the next approximation ϕ^{n+1} can be directly obtained as ϕ_2 by

$$\phi^{n+1} = \phi^n + \Delta t\left[b_1 f(\phi_1) + b_2 f(\phi_2)\right] + \Delta t\left[\hat{b}_0 g(\phi^n) + \hat{b}_1 g(\phi_1)\right]. \tag{25}$$

In a similar manner, CSRK$(3, \gamma)$ can be constructed using (22).

To demonstrate the accuracy and stability of the CSRK methods, in the following section we simulate one-dimensional (1D) test problems with the zero Neumann boundary condition. The first numerical test compares the numerical stability of the linear convex splitting with that of the modified linear convex splitting. The second and third tests show the convergence result and energy stability for CSRK$(2, \gamma_\pm)$ and CSRK$(3, \gamma)$, respectively.

4.1. *CSRK$(2, \gamma_-)$ with modified linear convex splitting for the CH equation*

In convex splitting methods, we can choose nonlinear (5), linear (9), and various forms of energy splitting. In [23], the IMEX-RK methods of up to a third-order time accuracy using the linear convex splitting (LCS) (9) for the CH equation was presented. However, (9) does not preserve the convexity of $\Psi_c(\phi)$ and $\Psi_e(\phi)$ for $\phi < -1$ or $\phi > 1$. In order to emphasize an importance of convexity in the splitting, we consider a modified linear convex splitting (MLCS) [10] which preserves the convexity of $\Psi_c(\phi)$ and $\Psi_e(\phi)$ regardless of the value of ϕ,

$$\Psi(\phi) = \Psi_c(\phi) - \Psi_e(\phi) = \begin{cases} \left(\phi^2 + \dfrac{1}{4}\right) - \left(-2\phi - \dfrac{3}{4}\right) & \phi < -1,\\[2ex] \left(\phi^2 + \dfrac{1}{4}\right) - \left(\dfrac{3}{2}\phi^2 - \dfrac{1}{4}\phi^4\right) & \phi \in [-1, 1],\\[2ex] \left(\phi^2 + \dfrac{1}{4}\right) - \left(2\phi - \dfrac{3}{4}\right) & \phi > 1. \end{cases} \tag{26}$$

Fig. 2 shows the evolution of solution $\phi(x, t)$ obtained from (9) and (26) using CSRK$(2, \gamma_-)$ with two initial conditions $\phi(x, 0) = \text{rand}(x)$ and $3 \cdot \text{rand}(x)$ on a domain $\Omega = [0, 1]$. Here, $\epsilon = 0.01$, $\Delta x = 1/128$, $T_f = 2^{-6}$, and $\Delta t = T_f/2^4$. Although the magnitude of 3 is physically less meaningful for the initial condition, we choose it to consider a hypothetic situation of an unstable or blowup numerical solution at some computational steps. For the case of $\|\phi(x, 0)\|_\infty = 1$, both

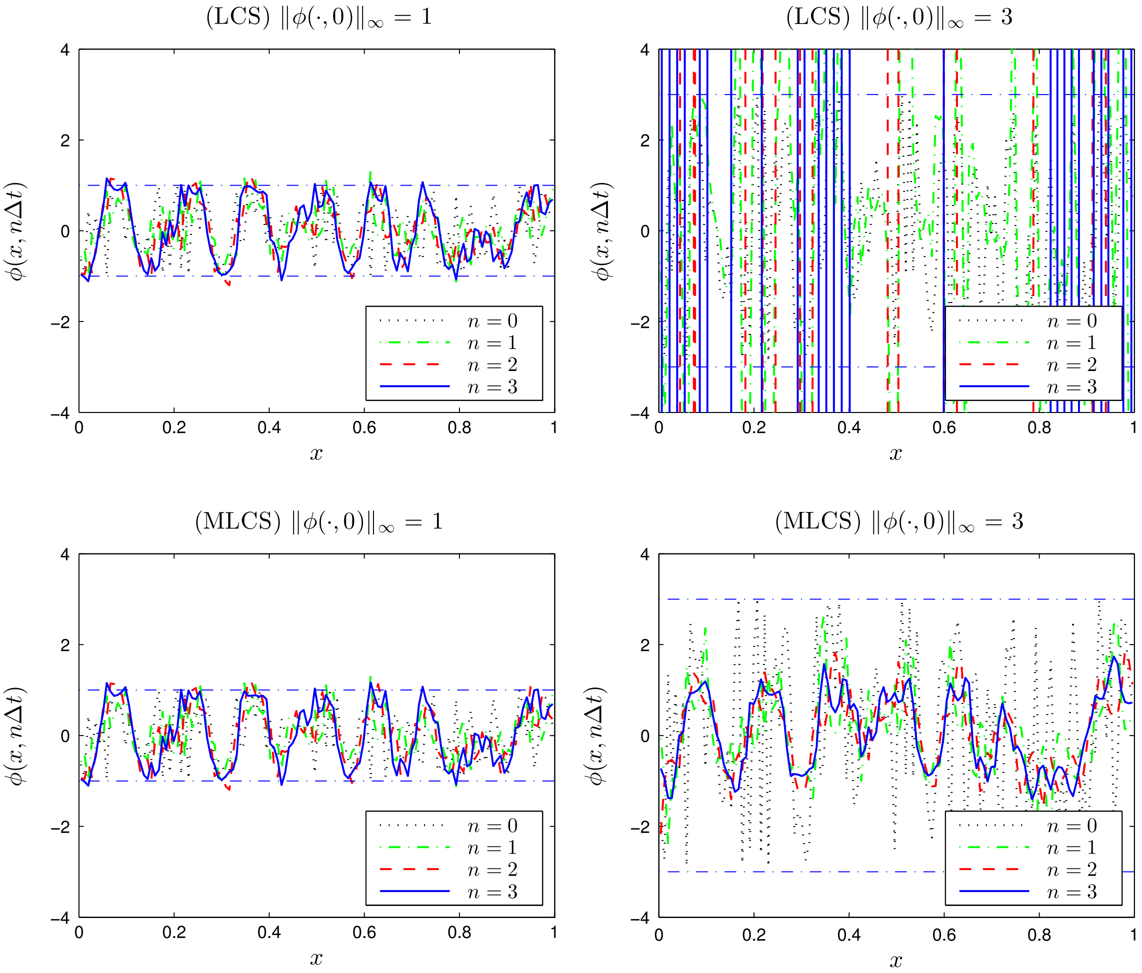

Fig. 2. Evolution of $\phi(x, t)$ at $t = n\Delta t = n \cdot 2^{-10}$ obtained by CSRK(2, γ_-) with the linear (9) and the modified linear (26) convex splittings using two initial conditions $\phi(x, 0) = \text{rand}(x)$ and $3 \cdot \text{rand}(x)$.

solutions by (9) and (26) are bounded. However, for the case of $\|\phi(x, 0)\|_\infty = 3$, the solution by (9) becomes unstable, whereas the solution by (26) becomes stable. This simple example shows that convexity of the splitting is crucial to ensure the stability of the CSRK methods.

4.2. Second-order convergence and energy stability of CSRK(2, $\gamma_\pm$)

To examine the stability of CSRK(2, $\gamma_\pm$), we calculate the relative l_2-error and evolution of the free energy functional by solving the AC and CH equations in a domain $\Omega = [0, 1]$. Here, for the numerical simulation, we set $\epsilon = 0.01$ and $\Delta x = 1/128$ and use the randomly perturbed initial condition $\phi(x, 0) = 0.001 \cdot \text{rand}(x)$. The numerical solution is evolved up to time $T_f = 1000$ and $T_f = 1000 \cdot \epsilon^2$ for the AC and CH equations, respectively.

Fig. 3 shows the numerical second-order convergence results at $t = T_f$ with the various time steps $\Delta t = T_f/2^{18}, T_f/2^{17}, \ldots, T_f/2^3$. Here, the error is computed by comparing with a quadruply over-resolved numerical solution obtained using CSRK(2, γ_-). It is clearly observed that the results of CSRK(2, $\gamma_\pm$) give the second-order of accuracy in time.

Fig. 4 illustrates the energy evolutions obtained by CSRK(2, γ_-) and CSRK(2, γ_+), with relatively large time steps $\Delta t = T_f/2^9, T_f/2^7, T_f/2^5, T_f/2^3$. Although the energy stability of CSRK(2, $\gamma_\pm$) has not yet been proven, the numerical results show that the energy is non-increasing for a large time step.

4.3. Gamma γ-dependency for convergence and energy stability of CSRK(3, γ)

We demonstrate the numerical convergence of CSRK(3, γ) for solving the AC and CH equations with $\epsilon = 0.01$, $\Delta x = 1/128$ which provides sufficient spatial accuracy, and an initial condition $\phi(x, 0) = 0.001 \cdot \text{rand}(x)$ on a domain $\Omega = [0, 1]$. The numerical solution is evolved to time $T_f = 100$ and $T_f = 100 \cdot \epsilon^2$ for the AC and CH equations, respectively.

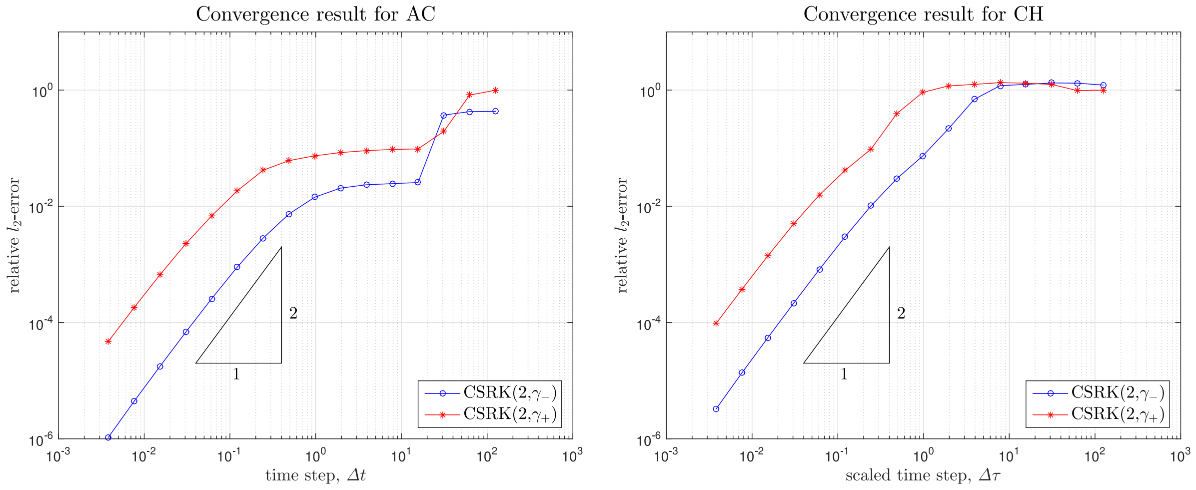

Fig. 3. Relative l_2-errors using CSRK(2, γ_-) and CSRK(2, γ_+) for the AC and CH equations. The scaled time step $\Delta\tau$ is defined as $\Delta\tau = \Delta t/\epsilon^2$ for the CH equation.

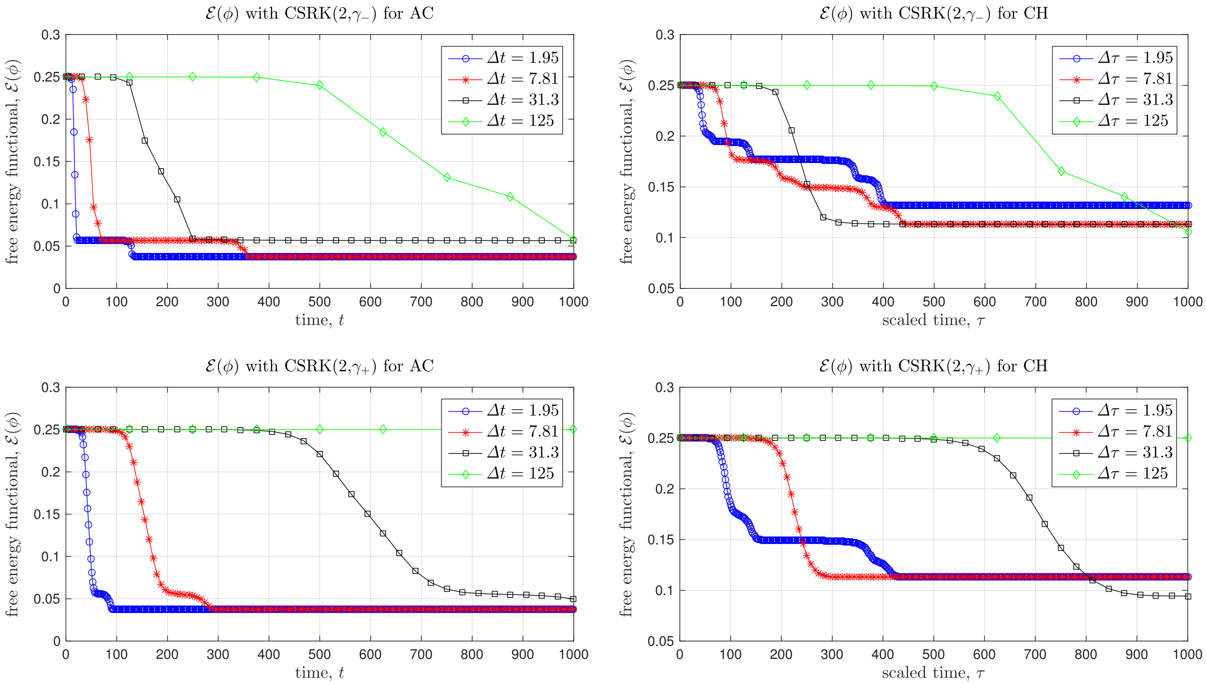

Fig. 4. Energy evolutions using CSRK(2, γ_-) and CSRK(2, γ_+) for the AC and CH equations. The scaled time τ is defined as $\tau = t/\epsilon^2$ for the CH equation.

Fig. 5 shows the relative l_2-errors with various time steps $\Delta t = T_f/2^{14}, T_f/2^{13}, \ldots, T_f$ and parameters $\gamma = 0.1, 0.3, 0.5, 0.7$ for the AC and CH equations. Here, the errors are computed by comparison with a quadruply over-resolved reference numerical solution of CSRK(3, $\gamma = 0.1$). We also show the error only when energy is non-increasing for the entire computational time. It is clearly observed that all cases give the third-order accuracy in time when the time step size is small enough.

However, the energy stability regions differ depending on γ. The first row of Fig. 6 shows the energy stability limit Δt_{stab} or $\Delta\tau_{\text{stab}}$ which is defined as the smallest time step size at which energy can increase at a certain time step. (We stop checking energy stability limit Δt_{stab} or $\Delta\tau_{\text{stab}}$ up to 100 and we just mark the limit at $\Delta t_{\text{stab}} = 200$ or $\Delta\tau_{\text{stab}} = 200$ when the method appears to be unconditionally stable.) The second row of Fig. 6 shows the relative l_2-errors when varying parameter γ with different time steps $\Delta t = T_f/2^{14}, T_f/2^{11}, T_f/2^{5}$. From the results shown in Figs. 5 and 6, we can conclude that third-order convergence of CSRK(3, γ) is always guaranteed for a small time step size. However, the energy stability region of CSRK(3, γ) strongly depends on the parameter γ and we need to select an appropriate value of γ for a given equation and parameter set.

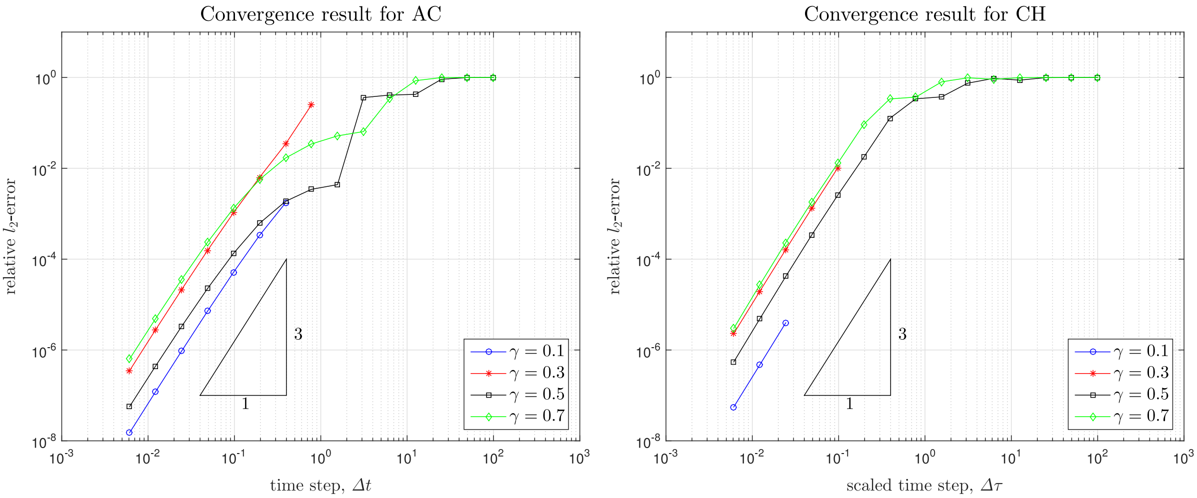

Fig. 5. Relative l_2-errors for various time steps and parameters γ using CSRK(3, γ) for the AC and CH equations.

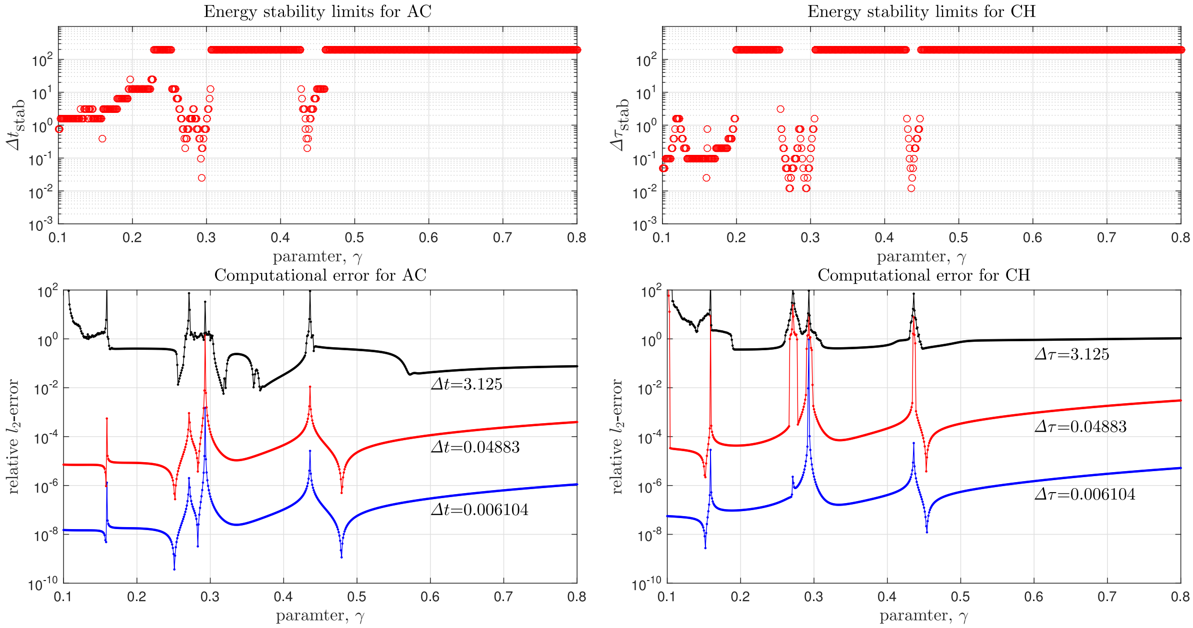

Fig. 6. Energy stability limits of time step with respect to γ (first row). Relative l_2-errors for γ with time steps $\Delta t = T_f/2^{14}, T_f/2^{11}, T_f/2^5$ (second row).

5. Numerical experiments

In this section, we present examples to numerically demonstrate the accuracy and efficiency of the proposed CSRK methods. The first numerical example shows the convergence result for a 1D test problem. The second and third examples show the spinodal decomposition with a randomly perturbed initial condition in 2D and 3D, respectively. We then apply CSRK(3, $\gamma = 1/3$) to the phase-field crystal equation and compute the growth of a polycrystal in a supercooled liquid in 3D in order to demonstrate the feasibility of the CSRK in computing the evolution of large systems.

5.1. Numerical convergence test with smooth initial data in 1D

We demonstrate the numerical convergence of the CSRK methods for solving the AC and CH equations with the zero Neumann boundary condition with the following initial condition on a domain $\Omega = [0, 1]$:

$$\phi(x, 0) = 0.01\cos(\pi x) + 0.25\cos(4\pi x) + 0.2\cos(11\pi x). \tag{27}$$

For the numerical simulations, $\epsilon = 0.01$ is used and the grid size is fixed to $\Delta x = 1/128$ which provides sufficient spatial accuracy. The numerical solution is evolved to time $T_f = 5$ and $T_f = 5 \cdot \epsilon^2$ for the AC and CH equations, respectively.

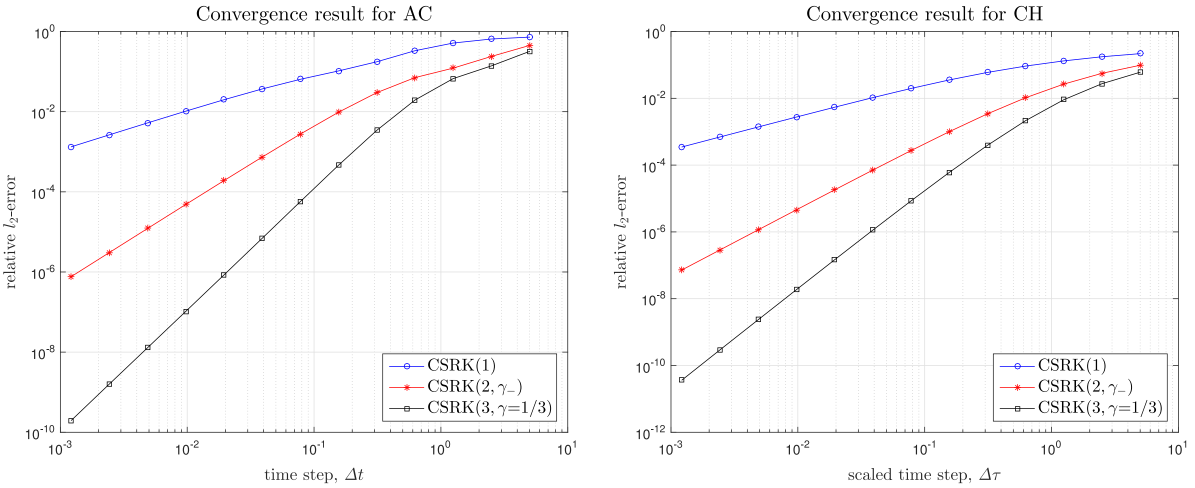

Fig. 7. Relative l_2-errors at $t = T_f$ for various time steps Δt in 1D. The scaled time step $\Delta\tau$ is defined as $\Delta\tau = \Delta t/\epsilon^2$.

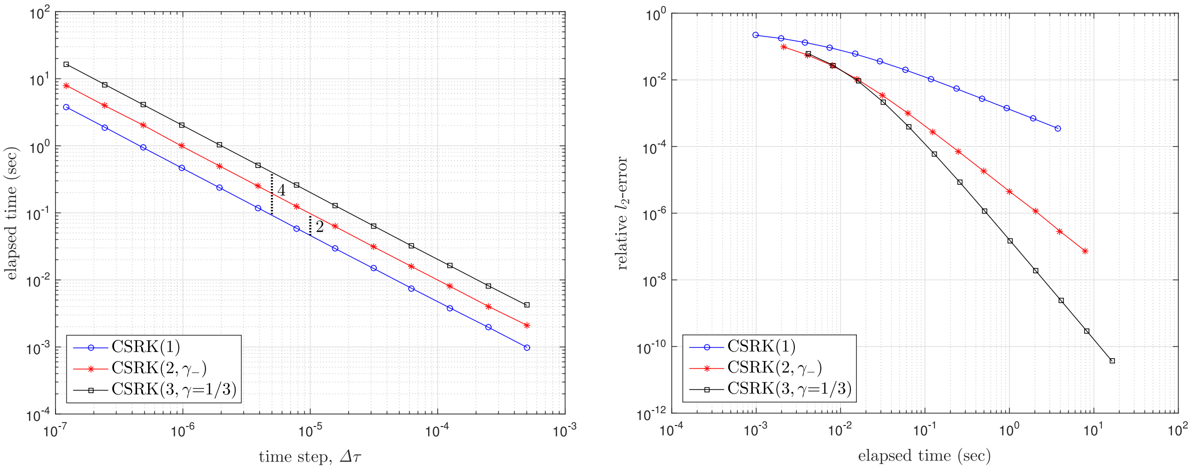

Fig. 8. Scalability and efficiency of the methods for various time steps $\Delta\tau$ in 1D.

Fig. 7 shows the relative l_2-errors with various time steps $\Delta t = T_f/2^{12}, T_f/2^{11}, \ldots, T_f$ for the AC and CH equations. Here, the errors are computed by comparison with a quadruply over-resolved reference numerical solution obtained using CSRK($3, \gamma = 1/3$). It is observed that the CSRK methods give the desired order accuracy in time.

Fig. 8 shows the elapsed time by MATLAB Ver 8.3 on a Linux machine with a couple of 2.4 GHz Xeon E5-2620 CPUs and 64GB memory for various time steps and corresponding relative l_2-errors to demonstrate the scalability and efficiency of the methods. Here, we only describe the case of the CH equation, since the AC equation shows a similar result. Compared to CSRK(1), we need almost 2-fold and 4-fold computational time for CSRK(2) and CSRK(3), respectively. Because the computational cost is linearly proportional to the number of stages, we expect the more efficient results of the higher order methods for a desired error. For a single digit error, CSRK(2) and CSRK(3) are already more efficient than CSRK(1). For more than two digits, CSRK(3) is the most efficient method.

5.2. Spinodal decomposition in 2D

We simulate the spinodal decomposition in a domain $\Omega = [0, 1] \times [0, 1]$ with the zero Neumann boundary condition, which is a typical example of the AC and CH equations. For the numerical simulations, we set the space steps $\Delta x = \Delta y = 1/128$ and $\epsilon = 0.01$. The initial state is a random perturbation where the average is zero and the amplitude is 0.001: $\phi(x, y, 0) = 0.001 \cdot \text{rand}(x, y)$. The final time is $T_f = 100$ and $T_f = 100 \cdot \epsilon^2$ for the AC and CH equations, respectively.

Fig. 9 shows the time evolution of the reference solutions for the AC and CH equations by CSRK($3, \gamma = 1/3$) with $\Delta t = T_f/2^{16}$. In the case of the evolution of the CH equation, after the phase separation, the coarsening evolution follows, which shows a highly inter-connected pattern. In each snapshot, the red, green, and blue regions indicate $\phi = 1, 0$, and -1, respectively, and the numerical times are shown on the bottom of the subplots.

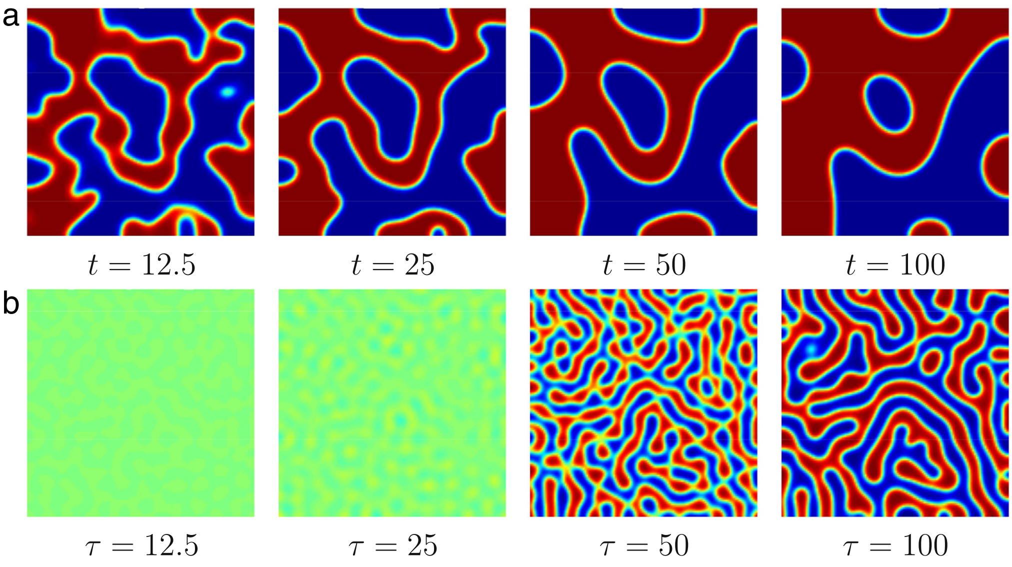

Fig. 9. Evolution of the order parameter ϕ for the (a) AC and (b) CH equations. The scaled time τ is defined as $\tau = t/\epsilon^2$.

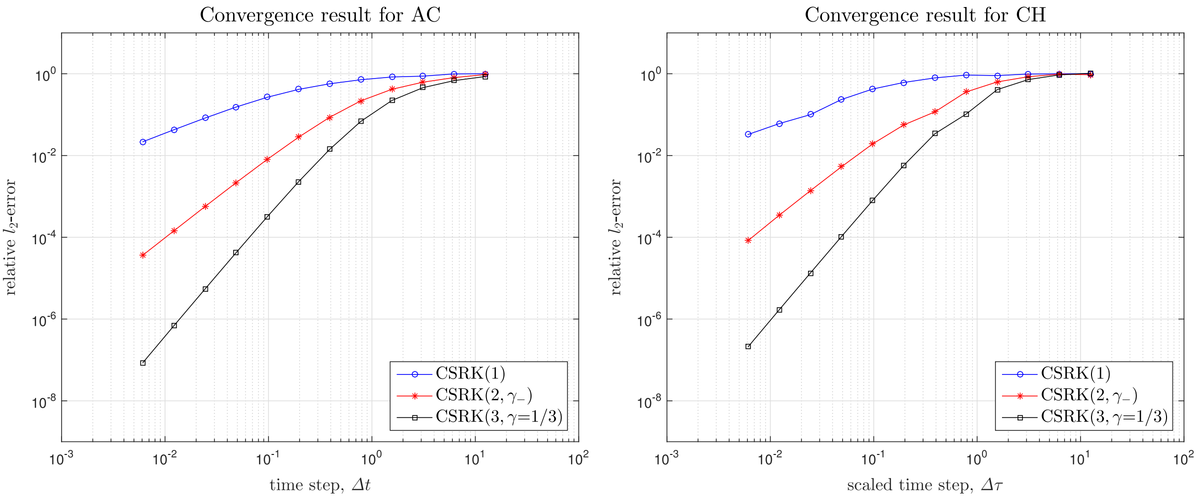

Fig. 10. Relative l_2-errors at $t = T_f$ for various time steps Δt in 2D.

Fig. 10 shows the numerical convergence of the CSRK methods at the final time T_f with the various time steps $\Delta t = T_f/2^{14}, T_f/2^{13}, \ldots, T_f/2^3$. Here, the errors are computed by comparison with the quadruply over-resolved reference numerical solution shown in Fig. 9. It is observed that the CSRK methods give desired order accuracy in time for the 2D problem.

5.3. Long-time simulation of the spinodal decomposition in 3D

We simulate the spinodal decomposition for the CH equation in a domain $\Omega = [0, 1]^3$ with the periodic boundary condition. For the numerical simulation, we set the space steps $\Delta x = \Delta y = \Delta z = 1/64$ and $\epsilon = 0.02$. The initial state is $\phi(x, y, z, 0) = 0.5 + 0.001 \cdot \mathrm{rand}(x, y, z)$, a small random perturbation from the 75% average concentration between $[-1, 1]$.

In Fig. 11, we present snapshots of the isosurfaces of ϕ solved by CSRK(3, $\gamma = 1/3$) with $\Delta t = \epsilon^2/8$. In each snapshot, the red, green, and blue regions indicate $\phi = 0.3$, 0, and -0.3, respectively. The randomly perturbed initial state is nucleated in the early stage. As the remaining regions grow, the evolution finally leads to a single sphere which is a numerical equilibrium state of this example problem.

Fig. 12 shows the energy dissipation property of the CH equation with the various time steps $\Delta t = 2\cdot\epsilon^2, 2^3\cdot\epsilon^2, \ldots, 2^9\cdot\epsilon^2$. Even when large time steps are used, the energy evolution shows the energy dissipation. This simulation provides the

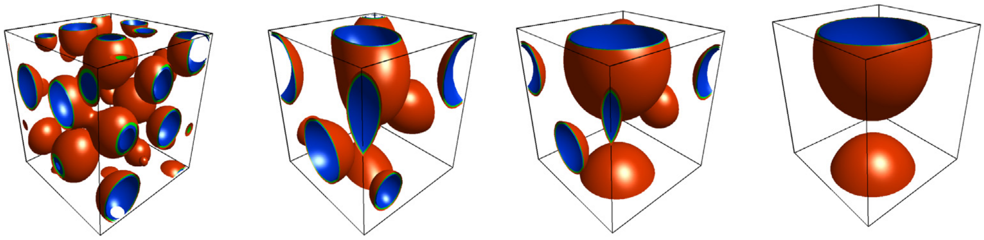

$t = 0.25$ $t = 0.75$ $t = 1.5$ $t = 3$

Fig. 11. Evolution of ϕ for the CH equation. The times are shown below each figure.

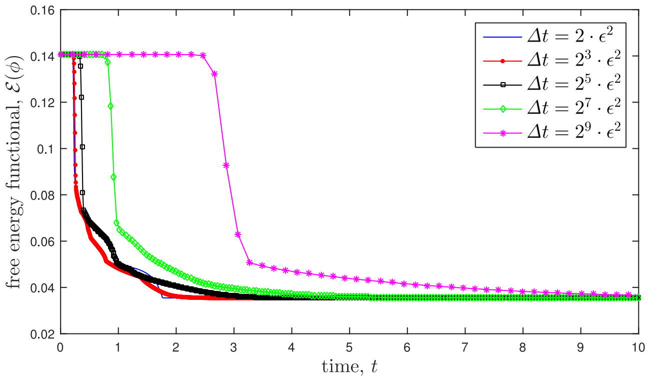

Fig. 12. Energy evolution for the CH equation solved by CSRK(3, $\gamma = 1/3$) with the various time steps $\Delta t = 2 \cdot \epsilon^2, 2^3 \cdot \epsilon^2, \ldots, 2^9 \cdot \epsilon^2$.

numerical evidence that CSRK methods have good energy stability, even though the strong energy stability has not yet been established.

5.4. Application to the phase-field crystal equation in 3D

The phase-field crystal (PFC) equation is a model for the microstructural evolution of two-phase systems on atomic length and diffusive time scales [25]. The Swift–Hohenberg free energy functional [26] is

$$\mathcal{E}_{\mathrm{PFC}}(\phi) := \int_{\Omega} \left(\frac{1}{4}\phi^4 + \frac{1-\epsilon}{2}\phi^2 - |\nabla \phi|^2 + \frac{1}{2}(\Delta \phi)^2 \right) d\mathbf{x}, \tag{28}$$

where $\phi : \Omega \subset \mathbb{R}^d \to \mathbb{R}$ ($d = 1, 2, 3$) is the density field and ϵ is a positive constant with physical significance. The PFC equation is derived from the gradient flow for (28) under the H^{-1} inner product

$$\frac{\partial \phi}{\partial t} = \Delta(\phi^3 + (1-\epsilon)\phi + 2\Delta\phi + \Delta^2\phi), \tag{29}$$

where we assume that ϕ is periodic on Ω. Because the equation is the gradient type, it can readily be seen that the energy functional $\mathcal{E}_{\mathrm{PFC}}(\phi)$ is non-increasing in time.

The PFC equation is a sixth-order nonlinear partial differential equation and thus it is generally not easy to obtain an analytic solution. In order to solve the PFC equation accurately and efficiently, we first split $\mathcal{E}_{\mathrm{PFC}}(\phi)$ as follows:

$$\begin{aligned} \mathcal{E}_{\mathrm{PFC}}(\phi) &= \int_{\Omega} \left(\frac{\beta}{2}\phi^2 + \frac{1}{2}(\Delta\phi)^2 \right) d\mathbf{x} - \int_{\Omega} \left(-\frac{1}{4}\phi^4 + \frac{\beta - 1 + \epsilon}{2}\phi^2 + |\nabla\phi|^2 \right) d\mathbf{x}, \\ &= \mathcal{E}^c_{\mathrm{PFC}}(\phi) - \mathcal{E}^e_{\mathrm{PFC}}(\phi), \end{aligned}$$

where $\mathcal{E}^c_{\mathrm{PFC}}$ and $\mathcal{E}^e_{\mathrm{PFC}}$ are convex for $|\phi| < \sqrt{(\beta - 1 + \epsilon)/3}$. Note that, while the larger β renders CSRK more stable, CSRK may lose computational precision. We then apply CSRK(3, $\gamma = 1/3$) to the PFC equation with $\beta = 4$,

$$\begin{aligned} \frac{\partial \phi}{\partial t} &= \left(\beta\Delta\phi + \Delta^3\phi\right) + \left(\Delta(\phi^3 - (\beta - 1 + \epsilon)\phi) + 2\Delta^2\phi\right), \\ &= f(\phi) + g(\phi). \end{aligned} \tag{30}$$

Fig. 13 shows the numerical simulation of crystal growth in three dimensions. We simulate the growth and interaction of two crystallites that originate from two nucleation sites. The computational domain is $\Omega = [0, 128]^3$, and we assume

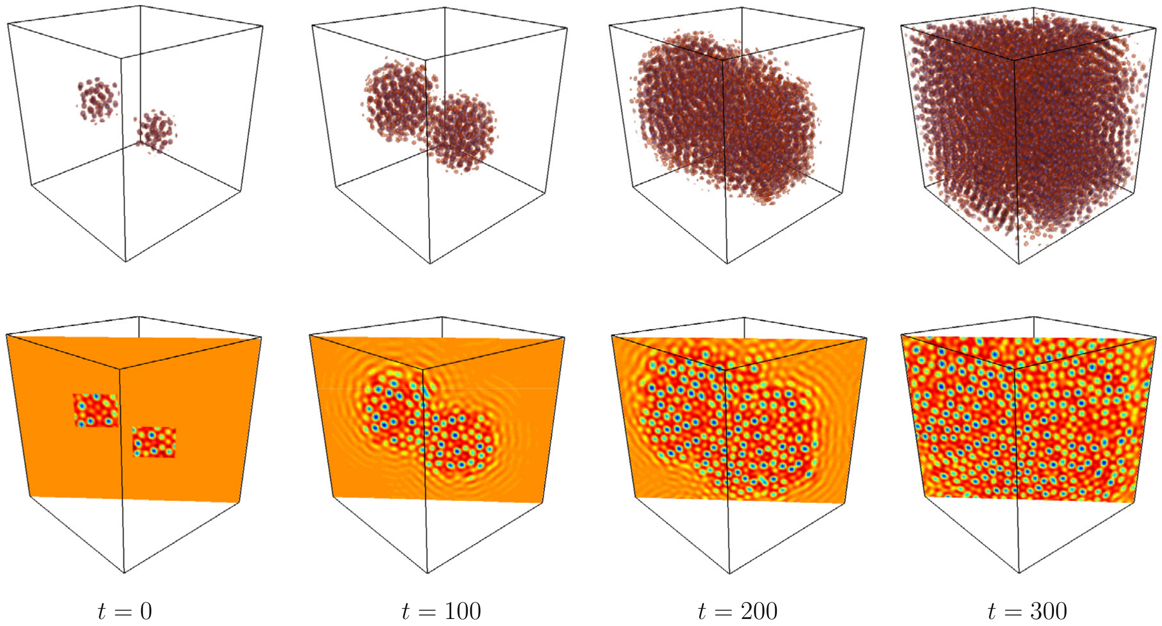

Fig. 13. Crystal growth in a supercooled liquid in 3D. The first row shows isosurfaces of the solution, while the second row presents a slice of the solution across a plane. The times are shown below each figure. (For interpretation of the references to color in this figure legend, the reader is referred to the web version of this article.) .

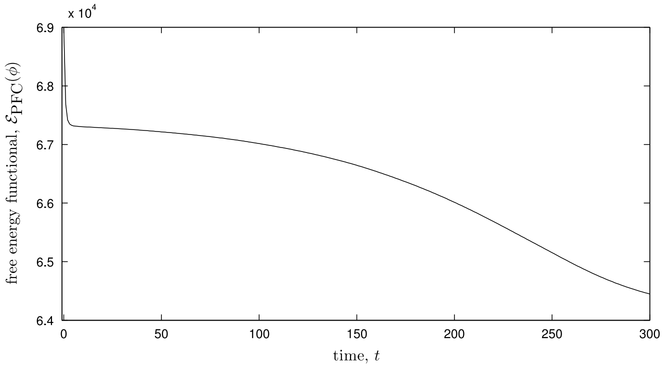

Fig. 14. Energy evolution for the PFC equation.

periodic boundary conditions in all directions. For this calculation, we employ $\epsilon = 0.25$, a uniform mesh $\Delta x = \Delta y = \Delta z = 1$, and $\Delta t = 1$.

The initial configuration is generated as follows. We let a randomly perturbed constant (liquid) state evolve to a periodic lattice (solid) state, $\phi(x, y, z, 0) = 0.285 + 0.1 \cdot \mathrm{rand}(x, y, z)$. We extract two subregions of the numerical solutions at $t = 1000$ with a hexahedric shape, and superpose them to a constant density field $\phi = 0.285$. The first row in Fig. 13 shows the isosurfaces of the density field, while the second row presents a slice of the solution across the indicated plane. In each slice, the red, green, and blue regions indicate $\phi = 0.6835$, -0.0342, and -0.7519, respectively. Similar computation results can be found in [16,9,18].

Fig. 14 shows the time evolution of the energy functional $\mathcal{E}_{\mathrm{PFC}}(\phi)$. It is clearly shown that the energy is non-increasing with time, whereby the numerical result is energy stable.

6. Conclusions

The first-order convex splitting scheme has been well known in the field of numerical methods for the phase-field models. Even though the convex splitting concept seems to be compatible with the framework of implicit–explicit Runge–Kutta (IMEX-RK) methods, the combining of the two concepts is not popular in the phase-field research community.

In this paper, we presented the first, second, and some special cases of the third-order Convex Splitting Runge–Kutta (CSRK) methods for solving phase-field models such as the Allen–Cahn, Cahn–Hilliard, and phase-field crystal equations.

Practically, convex splitting has many possibilities and we specifically investigated the efficiency and feasibility of nonlinear, modified linear, and classical linear convex splitting methods. We also numerically tested the CSRK methods with linear convex splitting using some of typical examples.

Because the CSRK schemes are based on the RK scheme, the time accuracy is clearly verified and can be easily extended to the high-order accuracy. Expecting that the convex splitting positively affects the stability, we numerically investigated the energy stability of CSRK methods. We observed that some CSRK methods preserve the energy stability for practically large time steps, even though the convex splitting itself is not sufficient. Unlike time accuracy, the unconditional energy stability has not yet been theoretically guaranteed, except for the CSRK(1) method. However, the significant improvement of the energy stability was observed for some of the methods. Therefore, investigating a way to improve and mathematically prove the energy stability will be valuable. We have a plan to present the proof of energy stability for high order CSRK methods in near future.

Acknowledgments

This research was supported by the Basic Science Research Program through the National Research Foundation of Korea (NRF) funded by Ministry of Education (MOE) and Ministry of Science and ICT and Future Planning (MSIP) (2009-0093827, 2015-003037).

Appendix A. Order conditions for implicit–explicit Runge–Kutta method

We now describe the derivation and order conditions up to the third-order accuracy for implicit–explicit Runge–Kutta (IMEX-RK) methods. Various explanations for the order conditions of Runge–Kutta (RK) methods can be found in [22,27], which present the derivations of the solutions and relations between the tree and elementary differentials to understand the order conditions. In this work, we seek to understand the order conditions by only using the matrix multiplication and the Taylor expansion.

We assume that the coefficients $(\mathbf{c}, \mathbf{A}, \mathbf{b})$ and $(\hat{\mathbf{c}}, \hat{\mathbf{A}}, \hat{\mathbf{b}})$ satisfy the conditions $\mathbf{c} = \mathbf{A}\mathbf{1}$, $\mathbf{b}\cdot\mathbf{1} = 1$, $\hat{\mathbf{c}} = \hat{\mathbf{A}}\mathbf{1}$, and $\hat{\mathbf{b}}\cdot\mathbf{1} = 1$. Note that, from these assumptions, analyzing the order conditions for an autonomous system is sufficient for non-autonomous systems $y_t(t) = f(t, y) + g(t, y)$ [28].

The Taylor expansion of the exact solution of system (11) can be written in terms of the elementary differentials as

$$y(h) = y_0 + h(f+g) + \frac{h^2}{2}(f'+g')(f+g) + \frac{h^3}{6}(f''+g'')(f+g)^2 + \frac{h^3}{6}(f'+g')^2(f+g) + O(h^4), \tag{31}$$

where all function values of f, g, and their derivatives are evaluated at y_0. From (16), the Taylor expansion of the RK solution after one step can now be given by

$$y(h) = y_0 + h(\mathbf{b}\cdot\mathbf{k} + \hat{\mathbf{b}}\cdot\hat{\mathbf{k}}), \tag{32}$$

where

$$\mathbf{k} = f\mathbf{1} + h\mathbf{c}ff' + h\hat{\mathbf{c}}gf' + \frac{1}{2}h^2(\mathbf{c}f + \hat{\mathbf{c}}g)^2 f'' + h^2\mathbf{A}(\mathbf{c}f + \hat{\mathbf{c}}g)f'f' + h^2\hat{\mathbf{A}}(\mathbf{c}f + \hat{\mathbf{c}}g)g'f' + O(h^3), \tag{33}$$

$$\hat{\mathbf{k}} = g\mathbf{1} + h\mathbf{c}fg' + h\hat{\mathbf{c}}gg' + \frac{1}{2}h^2(\mathbf{c}f + \hat{\mathbf{c}}g)^2 g'' + h^2\mathbf{A}(\mathbf{c}f + \hat{\mathbf{c}}g)f'g' + h^2\hat{\mathbf{A}}(\mathbf{c}f + \hat{\mathbf{c}}g)g'g' + O(h^3). \tag{34}$$

By equating the coefficients of the elementary differential (31) with the Taylor expansion (32), we can obtain the order conditions (Table 1). Conditions of the second and third columns of Table 1 are the standard order conditions for each table to satisfy the accuracy. Conditions of the fourth column of Table 1 arise because of the coupling of the two schemes. Note that the conditions $\mathbf{b}\cdot\hat{\mathbf{A}}\mathbf{c} = \hat{\mathbf{b}}\cdot\mathbf{A}\mathbf{c} = 1/6$ and $\mathbf{b}\cdot\hat{\mathbf{A}}\hat{\mathbf{c}} = \hat{\mathbf{b}}\cdot\mathbf{A}\hat{\mathbf{c}} = 1/6$ can be used instead of the compact conditions $\mathbf{b}\cdot\hat{\mathbf{A}}\mathbf{c} + \hat{\mathbf{b}}\cdot\mathbf{A}\mathbf{c} = 1/3$ and $\mathbf{b}\cdot\hat{\mathbf{A}}\hat{\mathbf{c}} + \hat{\mathbf{b}}\cdot\mathbf{A}\hat{\mathbf{c}} = 1/3$, because a solution might be easier to find from the system of algebraic equations.

Appendix B. Some specific examples for implicit–explicit Runge–Kutta method

In this appendix, we describe the Butcher tables for IMEX-RK schemes up to the third-order. We can find other tables that are not introduced in this appendix, since we do not deal with all cases for IMEX-RK tables. As mentioned in Section 3, we consider the three additional conditions as follows:

$$\mathbf{c} = \hat{\mathbf{c}}, \tag{35}$$

$$a_{ii} = \gamma, \quad \text{for } i = 1, 2, \ldots, s, \tag{36}$$

$$b_i = a_{si} \quad \text{and} \quad \hat{b}_i = \hat{a}_{si}, \quad \text{for } i = 0, 1, \ldots, s. \tag{37}$$

Table 2
Order conditions for IMEX-RK methods up to the third order accuracy.

Order	Stand-alone conditions		Coupling conditions
	IM	EX	
1	$\mathbf{b}\cdot\mathbf{1}=1$	$\hat{\mathbf{b}}\cdot\mathbf{1}=1$	–
2	$\mathbf{b}\cdot\mathbf{c}=1/2$	$\hat{\mathbf{b}}\cdot\mathbf{c}=1/2$	–
3	$\mathbf{b}\cdot\mathbf{c}^2=1/3$ $\mathbf{b}\cdot\mathbf{Ac}=1/6$	$\hat{\mathbf{b}}\cdot\mathbf{c}^2=1/3$ $\hat{\mathbf{b}}\cdot\hat{\mathbf{A}}\mathbf{c}=1/6$	$\mathbf{b}\cdot\hat{\mathbf{A}}\mathbf{c}+\hat{\mathbf{b}}\cdot\mathbf{Ac}=1/3$

Because the condition (35) is added, we could reduce the massive order conditions (see Table 2).

First, we can represent the well-known semi-implicit schemes in the 1-stage IMEX-RK table. Note that this is a unique 1-stage IMEX-RK table satisfying the three additional conditions.

$$\begin{array}{c|cc} 0 & 0 & 0 \\ 1 & 0 & 1 \\ \hline & 0 & 1 \end{array} \qquad \begin{array}{c|cc} 0 & 0 & 0 \\ 1 & 1 & 0 \\ \hline & 1 & 0 \end{array} \tag{38}$$

Next, we consider the 2-stage IMEX-RK to obtain the second-order accuracy.

$$\begin{array}{c|ccc} 0 & 0 & 0 & 0 \\ \gamma & 0 & \gamma & 0 \\ 1 & 0 & b_1 & \gamma \\ \hline & 0 & b_1 & \gamma \end{array} \qquad \begin{array}{c|ccc} 0 & 0 & 0 & 0 \\ \gamma & \gamma & 0 & 0 \\ 1 & \hat{b}_0 & \hat{b}_1 & 0 \\ \hline & \hat{b}_0 & \hat{b}_1 & 0 \end{array} \tag{39}$$

where the coefficients γ, b_1, $\hat{b}_0$, and $\hat{b}_1$ satisfy the first- and second-order conditions

$$b_1+\gamma=1, \qquad \gamma b_1+\gamma=1/2, \qquad \hat{b}_0+\hat{b}_1=1, \qquad \gamma\hat{b}_1=1/2. \tag{40}$$

From the quadratic equation, $\gamma(1-\gamma)+\gamma=1/2$, we have $\gamma=(2\pm\sqrt{2})/2$. We then obtain $b_1=1-\gamma$, $\hat{b}_1=1/(2\gamma)$, and $\hat{b}_0=1-\hat{b}_1$. Note that the Butcher table (39) and these solutions are identical to those shown in the table in [24].

To develop the third-order accurate methods, we could consider the 3-stage IMEX-RK table. However, we could not find a pair consisting of a 3-stage SDIRK and ERK that satisfies the third-order accurate and additional conditions. We now consider a combination of 4-stage SDIRK and ERK methods.

$$\begin{array}{c|ccccc} 0 & 0 & 0 & 0 & 0 & 0 \\ \gamma & 0 & \gamma & 0 & 0 & 0 \\ c_2 & 0 & a_{21} & \gamma & 0 & 0 \\ c_3 & 0 & a_{31} & a_{32} & \gamma & 0 \\ 1 & 0 & b_1 & b_2 & b_3 & \gamma \\ \hline & 0 & b_1 & b_2 & b_3 & \gamma \end{array} \qquad \begin{array}{c|ccccc} 0 & 0 & 0 & 0 & 0 & 0 \\ \gamma & \gamma & 0 & 0 & 0 & 0 \\ c_2 & \hat{a}_{20} & \hat{a}_{21} & 0 & 0 & 0 \\ c_3 & \hat{a}_{30} & \hat{a}_{31} & \hat{a}_{32} & 0 & 0 \\ 1 & \hat{b}_0 & \hat{b}_1 & \hat{b}_2 & \hat{b}_3 & 0 \\ \hline & \hat{b}_0 & \hat{b}_1 & \hat{b}_2 & \hat{b}_3 & 0 \end{array} \tag{41}$$

Table 3 lists the order conditions up to the third order accuracy for the IMEX-RK table (41). The algebraic equations (Ta.3;1)–(Ta.3;4) and (Ta.3;5)–(Ta.3;8) are the standard order conditions for each table to satisfy the third-order accuracy. Also, (Ta.3;9) and (Ta.3;10) are the coupling conditions for constructing the IMEX-RK tables where we choose $\mathbf{b}\cdot\hat{\mathbf{A}}\mathbf{c}=1/6$ and $\hat{\mathbf{b}}\cdot\mathbf{Ac}=1/6$ instead of $\mathbf{b}\cdot\hat{\mathbf{A}}\mathbf{c}+\hat{\mathbf{b}}\cdot\mathbf{Ac}=1/3$. For example, we explain the derivation of (Ta.3;3). From the condition $\mathbf{b}\cdot\mathbf{c}^2=1/3$, we have

$$b_1\gamma^2+b_2c_2^2+b_3c_3^2+\gamma=1/3. \tag{42}$$

Using c_2' and c_3', we can rewrite (42) as

$$(b_1+b_2+b_3)\gamma^2+2\gamma(b_2c_2'+b_3c_3')+\gamma+(b_2c_2'^2+b_3c_3'^2)=1/3. \tag{43}$$

By using (Ta.3;1) and (Ta.3;2), we finally have $b_2c_2'^2+b_3c_3'^2=1/3-2\gamma+3\gamma^2-\gamma^3=p_3$.

An easy way to find four-stage IMEX-RK schemes is to construct a SDIRK first using (Ta.3;1)–(Ta.3;4). We then find $\hat{\mathbf{b}}$ using (Ta.3;5)–(Ta.3;7) and (Ta.3;10). Finally $\hat{a}_{21}$, $\hat{a}_{31}$, and $\hat{a}_{32}$ are obtained using (Ta.3;8) and (Ta.3;9), and $\hat{a}_{20}$, $\hat{a}_{30}$ are then obtained.

Table 3
Algebraic equations to satisfy the third-order condition for (41).

Matrix form	Algebraic form	
$\mathbf{b}\cdot\mathbf{1}=1$	$b_1+b_2+b_3=p_1$	(Ta.3;1)
$\mathbf{b}\cdot\mathbf{c}=1/2$	$b_2c_2'+b_3c_3'=p_2$	(Ta.3;2)
$\mathbf{b}\cdot\mathbf{c}^2=1/3$	$b_2c_2'^2+b_3c_3'^2=p_3$	(Ta.3;3)
$\mathbf{b}\cdot\mathbf{Ac}=1/6$	$b_3a_{32}c_2'=p_4$	(Ta.3;4)
$\hat{\mathbf{b}}\cdot\mathbf{1}=1$	$\hat{b}_0+\hat{b}_1+\hat{b}_2+\hat{b}_3=1$	(Ta.3;5)
$\hat{\mathbf{b}}\cdot\mathbf{c}=1/2$	$\hat{b}_1\gamma+\hat{b}_2c_2+\hat{b}_3c_3=1/2$	(Ta.3;6)
$\hat{\mathbf{b}}\cdot\mathbf{c}^2=1/3$	$\hat{b}_1\gamma^2+\hat{b}_2c_2^2+\hat{b}_3c_3^2=1/3$	(Ta.3;7)
$\hat{\mathbf{b}}\cdot\hat{\mathbf{A}}\mathbf{c}=1/6$	$\hat{b}_2\hat{a}_{21}\gamma+\hat{b}_3(\hat{a}_{31}\gamma+\hat{a}_{32}c_2)=1/6$	(Ta.3;8)
$\mathbf{b}\cdot\hat{\mathbf{A}}\mathbf{c}=1/6$	$b_2\hat{a}_{21}\gamma+b_3(\hat{a}_{31}\gamma+\hat{a}_{32}c_2)=q_1$	(Ta.3;9)
$\hat{\mathbf{b}}\cdot\mathbf{Ac}=1/6$	$\hat{b}_2a_{21}\gamma+\hat{b}_3(a_{31}\gamma+a_{32}c_2)=q_1$	(Ta.3;10)
$p_1=1-\gamma$	$q_1=1/6-\gamma/2$	
$p_2=1/2-2\gamma+\gamma^2$	$c_2'=c_2-\gamma$	
$p_3=1/3-2\gamma+3\gamma^2-\gamma^3$	$c_3'=c_3-\gamma$	
$p_4=1/6-3\gamma/2+3\gamma^2-\gamma^3$		

We introduce an algorithm for constructing the four-stage third-order SDIRK methods, choosing c_1 and b_3 as free parameters with $c_1=c_3$. We should note that there are other algorithms using a different set of free parameters.

Algorithm for SDIRK

(a) Choose $c_1=c_3=\gamma\neq 0$ and $b_3\neq 0$ with $c_2\neq c_1$ and $b_2\neq 0$.

(b) $c_2'=p_3/p_2$, $b_2=p_2/c_2'$, $b_1=p_1-b_2-b_3$, $a_{32}=p_4/(b_3c_2')$, $a_{31}=c_3'-a_{32}$, and $a_{21}=c_2'$.

After constructing the SDIRK table for an implicit term, we construct the table for the explicit term considering the standard and coupling order conditions.

Algorithm for ERK using a given SDIRK

(a) $\hat{b}_1$, $\hat{b}_2$, $\hat{b}_3$ from the linear system (Ta.3;6), (Ta.3;7), and (Ta.3;10).

(b) $\hat{b}_0=1-\hat{b}_1-\hat{b}_2-\hat{b}_3$.

(c) If $b_3\hat{b}_2-b_2\hat{b}_3\neq 0$, $\hat{a}_{21}=\frac{b_3+(3\gamma-1)\hat{b}_3}{6\gamma(b_3\hat{b}_2-b_2\hat{b}_3)}$ and $\hat{a}_{20}=c_2-\hat{a}_{21}$.

(d) Choosing $\hat{a}_{32}$ as a free parameter, $\hat{a}_{31}=\frac{1/6-\hat{b}_2\hat{a}_{21}\gamma-\hat{b}_3\hat{a}_{32}c_2}{\hat{b}_3\gamma}$ and $\hat{a}_{30}=c_3-\hat{a}_{31}-\hat{a}_{32}$.

The table constructed by using the algorithms for SDIRK and ERK choosing $c_1=c_3=b_3=\gamma$ is the one parameter family, IMEX-RK$(3,\gamma)$, introduced in Section 3.

References

[1] S.M. Allen, J.W. Cahn, A microscopic theory for antiphase boundary motion and its application to antiphase domain coarsening, Acta Metall. 27 (6) (1979) 1085–1095.
[2] J.W. Cahn, J.E. Hilliard, Free energy of a nonuniform system. I. Interfacial free energy, J. Chem. Phys. 28 (2) (1958) 258–267.
[3] V. Badalassi, H. Ceniceros, S. Banerjee, Computation of multiphase systems with phase field models, J. Comput. Phys. 190 (2) (2003) 371–397.
[4] L.-Q. Chen, Phase-field models for microstructure evolution, Annu. Rev. Mater. Sci. 32 (1) (2002) 113–140.
[5] C.M. Elliott, A. Stuart, The global dynamics of discrete semilinear parabolic equations, SIAM J. Numer. Anal. 30 (6) (1993) 1622–1663.
[6] D.J. Eyre, An unconditionally stable one-step scheme for gradient systems, Unpublished article.
[7] Z. Hu, S.M. Wise, C. Wang, J.S. Lowengrub, Stable and efficient finite-difference nonlinear-multigrid schemes for the phase field crystal equation, J. Comput. Phys. 228 (15) (2009) 5323–5339.
[8] Z. Guan, J.S. Lowengrub, C. Wang, S.M. Wise, Second order convex splitting schemes for periodic nonlocal Cahn–Hilliard and Allen–Cahn equations, J. Comput. Phys. 277 (2014) 48–71.
[9] J. Shin, H.G. Lee, J.-Y. Lee, First and second order numerical methods based on a new convex splitting for phase-field crystal equation, J. Comput. Phys. 327 (2016) 519–542.
[10] X. Wu, G. Zwieten, K. Zee, Stabilized second-order convex splitting schemes for Cahn–Hilliard models with application to diffuse-interface tumor-growth models, Int. J. Numer. Methods Biomed. Eng. 30 (2) (2014) 180–203.
[11] P. Vignal, L. Dalcin, D.L. Brown, N. Collier, V.M. Calo, An energy-stable convex splitting for the phase-field crystal equation, Comput. Struct. 158 (1) (2015) 355–368.
[12] D. Furihata, A stable and conservative finite difference scheme for the Cahn–Hilliard equation, Numer. Math. 87 (4) (2001) 675–699.
[13] J. Kim, A numerical method for the Cahn–Hilliard equation with a variable mobility, Commun. Nonlinear Sci. Numer. Simul. 12 (8) (2007) 1560–1571.
[14] L. Cueto-Felgueroso, J. Peraire, A time-adaptive finite volume method for the Cahn–Hilliard and Kuramoto–Sivashinsky equations, J. Comput. Phys. 227 (24) (2008) 9985–10017.
[15] X. Feng, T. Tang, J. Yang, Long time numerical simulations for phase-field problems using p-adaptive spectral deferred correction methods, SIAM J. Sci. Comput. 37 (1) (2015) A271–A294.
[16] H.G. Lee, J. Shin, J.-Y. Lee, First and second order operator splitting methods for the phase field crystal equation, J. Comput. Phys. 299 (2015) 82–91.
[17] X. Feng, H. Song, T. Tang, J. Yang, Nonlinear stability of the implicit-explicit methods for the Allen–Cahn equation, Inverse Probl. Imaging 7 (3) (2013) 679–695.
[18] H. Gomez, X. Nogueira, An unconditionally energy-stable method for the phase field crystal equation, Comput. Methods Appl. Mech. Engrg. 249 (2012) 52–61.
[19] H.G. Lee, J.-Y. Lee, A semi-analytical fourier spectral method for the Allen–Cahn equation, Comput. Math. Appl. 68 (3) (2014) 174–184.
[20] U.M. Ascher, S.J. Ruuth, R.J. Spiteri, Implicit-explicit Runge–Kutta methods for time-dependent partial differential equations, Appl. Numer. Math. 25 (2) (1997) 151–167.
[21] C. Kennedy, M. Carpenter, Additive Runge–Kutta schemes for convection–diffusion-reaction equations, Appl. Numer. Math. 44 (1–2) (2003) 139–181.

[22] G. Wanner, E. Hairer, Solving Ordinary Differential Equations II, Vol. 1, Springer-Verlag, Berlin, 1991.
[23] H. Song, Energy stable and large time-stepping methods for the Cahn–Hilliard equation, Int. J. Comput. Math. 92 (10) (2015) 2091–2108.
[24] U.M. Ascher, S.J. Ruuth, B.T. Wetton, Implicit-explicit methods for time-dependent partial differential equations, SIAM J. Numer. Anal. 32 (3) (1995) 797–823.
[25] K. Elder, M. Katakowski, M. Haataja, M. Grant, Modeling elasticity in crystal growth, Phys. Rev. Lett. 88 (24) (2002) 245701.
[26] J. Swift, P.C. Hohenberg, Hydrodynamic fluctuations at the convective instability, Phys. Rev. A 15 (1) (1977) 319.
[27] E. Hairer, S.P. Norsett, G. Wanner, Solving Ordinary Differential Equations I. Nonstiff Problems, Vol. 8, Springer-Verlag, Berlin, 1993.
[28] L. Pareschi, G. Russo, Implicit-explicit Runge–Kutta schemes for stiff systems of differential equations, Recent Trends Numer. Anal. 3 (2000) 269–289.